

See discussions, stats, and author profiles for this publication at: <https://www.researchgate.net/publication/51762139>

Surface Heterogeneity on Hemispheres-in-Cell Model Yields All Experimentally-Observed Non-Straining Colloid Retention Mechanisms in Porous Media in the Presence of Energy Barriers

ARTICLE *in* LANGMUIR · NOVEMBER 2011

Impact Factor: 4.46 · DOI: 10.1021/la203587j · Source: PubMed

CITATIONS

28

READS

38

3 AUTHORS:



Huilian Ma

University of Utah

26 PUBLICATIONS 338 CITATIONS

SEE PROFILE



Eddy Pazmiño

University of Utah

15 PUBLICATIONS 155 CITATIONS

SEE PROFILE



William Paul Johnson

University of Utah

121 PUBLICATIONS 2,822 CITATIONS

SEE PROFILE

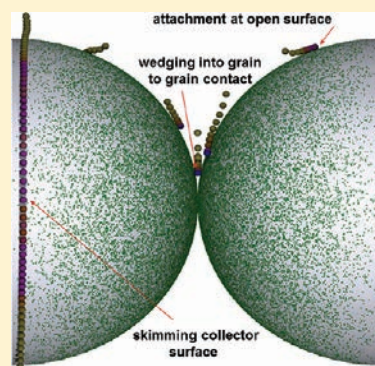
Surface Heterogeneity on Hemispheres-in-Cell Model Yields All Experimentally-Observed Non-Straining Colloid Retention Mechanisms in Porous Media in the Presence of Energy Barriers

Huilian Ma, Eddy Pazmino, and William P. Johnson*

Department of Geology and Geophysics, University of Utah, Salt Lake City, Utah 84112, United States

S Supporting Information

ABSTRACT: Many mechanisms of colloid retention in porous media under unfavorable conditions have been identified from experiments or theory, such as attachment at surface heterogeneities, wedging at grain to grain contacts, retention via secondary energy minimum association in zones of low flow drag, and straining in pore throats too small to pass. However, no previously published model is capable of representing all of these mechanisms of colloid retention. In this work, we demonstrate that incorporation of surface heterogeneity into our hemispheres-in-cell model yields all experimentally observed non-straining retention mechanisms in porous media under unfavorable conditions. We also demonstrate that the predominance of any given retention mechanism depends on the coupled colloid-collector-flow interactions that are governed by parameters such as the size and spatial frequency of heterogeneous attractive domains, colloid size, and solution ionic strength. The force/torque balance-simulated retention is shown to decrease gradually with decreasing solution ionic strength, in agreement with experimental observations. This gradual decrease stands in sharp contrast to predictions from mean field theory that does not account for discrete surface heterogeneity.



INTRODUCTION

While colloid retention in saturated granular porous media under favorable conditions (i.e., attractive colloid-collector interaction) is a well-established transport-limited process,^{1,2} retention of colloids under unfavorable conditions (i.e., repulsive colloid-collector interaction) is very complex, governed not only by particle transport to the surface, but also by the coupled colloid-collector-flow interactions near the collector surfaces.³ Hence, under unfavorable conditions, colloids are observed to move along the surface until they find a zone where colloid-collector-flow interaction allows their attachment.^{4,5} The contrast between favorable and unfavorable conditions is demonstrated in direct microscopic observation of colloid retention, with the former showing only instantaneous attachment upon interception of the surface with no re-entrainment, and the latter dominated by translation and/or rolling of colloids along the surface until they become attached or otherwise retained, or are re-entrained into the bulk solution.³

Models to predict colloid retention under unfavorable conditions take both empirical and mechanistic forms. Empirical correlation equations have been developed to predict colloid retention under unfavorable conditions;^{6–10} however, these predictions provide a range of applicability limited to the experimental conditions used to develop the regression, as well as highly limited insights into the underlying retention mechanisms. For instance, Chang and Chan¹⁰ recently proposed a correlation equation to predict α (attachment efficiency) based on trajectory (Brownian dynamics) simulations in a constricted tube network model.

Since the maximum repulsive energy barrier explored in their study was only 10 kT, which is a relatively small barrier that submicrometer colloids can easily overcome, this model cannot address the retention of colloids when subjected to the much greater energy barriers (100s to 1000s of kT) calculated for most environmental systems.

Mechanisms of colloid retention in porous media in the presence of energy barriers that are supported both by theory and by observation include the following: (i) attachment at surface heterogeneities (e.g., charge or topographic roughness) where repulsion is locally reduced or eliminated;^{11,12} (ii) wedging into grain to grain contacts;^{3,13,14} (iii) retention via secondary energy minima association in zones of low fluid drag;^{15,16} and (iv) straining in pore throats too small to pass.¹⁷ Here, the terms “straining” and “wedging” are used according to their conventional definitions; that is, the former describes retention in pore throats too small to pass, whereas the latter refers to retention at grain to grain contacts. It is critical to distinguish these two mechanisms because they have different dependencies on colloid size (relative to collector and pore throat size), fluid velocity, and repulsive energy barriers, as described in detail in Johnson et al.³ Although straining has been inferred in many column transport experiments for colloid-to-grain size ratios as low as 0.005, no direct observations are reported to support straining at these low colloid/collector ratios.³

Received: September 13, 2011

Revised: October 29, 2011

Published: November 01, 2011

Numerical simulations support direct attachment of colloids to surfaces via secondary energy minimum attraction, if one assumes that surface friction extends to the secondary energy minimum;¹⁸ however, observations have not been reported to support the geometrical arrangement of attached colloids expected from these simulations. Likewise, numerical simulations indicate that colloid retention can be expected in flow vortices;^{19,20} however, this mechanism was indicated to be relatively minor.²⁰ The dominance of any given established mechanism of colloid retention in porous media under unfavorable conditions depends on coupled colloid–collector–flow interactions. For example, Johnson et al.³ showed that under identical experimental conditions except colloid size, colloids greater than $2\ \mu\text{m}$ in diameter (colloid-to-collector ratio $> \sim 0.005$) were predominantly attached at grain to grain contacts (wedging), whereas colloids less than $2\ \mu\text{m}$ in diameter were primarily, and relatively randomly, deposited at the open surface away from grain contacts. The latter is consistent with retention via local reduction of repulsion via surface heterogeneity.

Existing mechanistic models for prediction of colloid retention under unfavorable conditions address particular mechanisms of retention described above; however, no previously published model is capable of representing all of these mechanisms of colloid retention. Colloid transport models already exist that simulate colloid attachment via nanoscale surface heterogeneity, such as heterogeneous surface charge^{21–24} or physical roughness,^{25,26} but these models do not account for the coupled effects of pore geometry and flow fields on colloidal retention (e.g., wedging at grain to grain contacts). Other models focus on the coupled pore geometry and fluid flow effects and can produce wedging in grain to grain contacts and retention in secondary energy minima in zones of low fluid drag,⁴ or retention in flow vortices.^{19,20} However, these models do not account for retention on the collector open surfaces via surface heterogeneity.

In this work, we demonstrate the simulation of all non-straining mechanisms of colloid retention under unfavorable conditions via incorporation of collector surface heterogeneity into the hemispheres-in-cell model^{27,28} (Figure 1), which capitalizes on the elegance of the Happel sphere-in-cell model by representing porous media of different porosities via adjusting the thickness of the fluid envelope relative to collector size. However, the hemispheres-in-cell model includes a grain to grain contact in which colloids may be wedged under unfavorable conditions. By incorporating surface charge heterogeneity into the hemispheres-in-cell model, retention of colloids via attachment on the open surface is simulated, thereby allowing this mechanistic force/torque balance model to simulate all known non-straining mechanisms of retention. Inclusion of attachment (immobilization) directly in secondary energy minima¹⁸ can also be simulated if one extends surface friction to distances from the surface as far as the secondary energy minimum. However, we believe that it is correct to restrict surface friction to separation distances less than the energy barrier maximum. Likewise, because the model is mechanistic it will be expected to produce retention in flow vortices for Reynolds numbers that produce vortices in the hemisphere-in-cell flow field.

Before we proceed, it is useful to discuss why straining is not represented in this model. Mechanistically, straining occurs when the colloid size is equal to or larger than the pore throat size, which occurs as a binary process that changes from inactive to active beyond a given colloid-to-pore throat size ratio. Since porous media generally show a range of pore throat sizes, the role

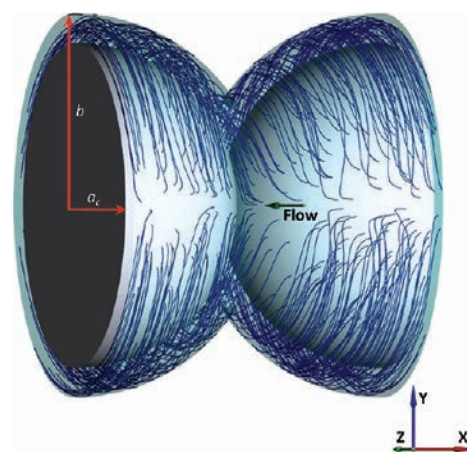


Figure 1. Hemispheres-in-cell model (3D representation) contains grain-to-grain contact and flow stagnation points and can represent a spectrum of porosities by varying the fluid shell thickness ($b - a_c$) (light sea green) relative to the collector radius (a_c) (blue). The flow is directed perpendicular to the line connecting the two hemisphere origins.

of straining in colloid retention needs to be addressed at the assemblage scale, e.g., in systems with a distribution of pore throat sizes, such as the random-packed spheres examined by Long and Hilpert.²⁹ However, it should also be noted that the simulations of Long and Hilpert were conducted solely under favorable conditions, and that simulating colloid retention under unfavorable conditions requires extremely small time and spatial steps in order to honor the energy barrier near the surface, such that simulations under unfavorable conditions become numerically intractable at the assemblage scale. This indicates the need for a hybrid approach that exports information from unit cell models into assemblage-scale flow fields and pore geometries. Such an approach will be the subject of future work, whereas in this paper we present unit cell simulation of colloid retention by non-straining mechanisms.

Using our mechanistic force/torque balance model, we demonstrate that the occurrence of all observed retention mechanisms is dependent upon the colloid–collector–flow interactions, which themselves depend on factors such as the size and surface properties of colloids and collectors, the solution chemistry, and the flow field. More specifically, we also explore how variations in attractive heterodomains (e.g., size, spatial frequency, and charge) influence colloid retention (and retention mechanism), and compare and contrast these simulations with relevant experiments and mean field models lacking discrete heterogeneity, where the measured zeta potentials are used to represent the mean-field (average) collector surface.

METHOD

Hemispheres-in-Cell Model Pore Domain Meshes and Fluid Flow Field. Computational meshes and fluid velocities for the pore domain of the hemispheres-in-cell model were generated and solved using *STAR-CD* and *STAR-CCM+* software (CD-adapco) by numerical simulation of the steady-state Navier–Stokes equation under laminar flow hydrodynamics. The resulting fluid field was coupled with a particle trajectory model (mechanistic force/torque balance). Detailed descriptions of the above components are provided in previous publications.^{27,28}

Colloidal Force Calculations Using Grid Surface Integration (GSI) Technique. Mechanistic models incorporating mean-field interaction forces between colloids and collector surfaces predict zero colloid attachment in the presence of significant repulsion, e.g., energy barriers greater than about 10 kT.^{30,31} However, colloid attachment is observed in experiments with much greater energy barriers, suggesting the need to replace mean-field with discrete interaction forces that account for nano- to micro- scale heterogeneities (e.g., charge or roughness) that may locally reduce or eliminate repulsion.

Discrete heterogeneity was incorporated into the hemispheres-in-cell model using the grid surface integration (GSI) technique, which was originally developed by Duffadar and Davis^{22,23} to replace mean field interaction with discrete interaction forces between spherical particles with heterogeneous planar surfaces. We adapted and extended the GSI technique to obtain discrete interaction forces between spherical colloids and spherical heterogeneous collector surfaces, as illustrated in Figure 2. Briefly, both the colloid and collector surfaces were discretized into small surface elements (approximated as planar elements). The interaction forces between each colloid surface element and each collector surface element were computed according to their respective surface potentials as described further below; and then these pairwise element interaction forces were summed to obtain the total interaction forces (F_{COLL}) between the colloid and the collector

$$F_{\text{COLL}} = \sum_{\text{particle}} \sum_{\text{collector}} [p(h)(\mathbf{e}_1 \cdot \mathbf{e}_0)](\mathbf{n}_s \cdot \mathbf{e}_0) dS \quad (1)$$

where \mathbf{e}_1 is the unit vector that specifies the direction between an element on the colloidal particle surface and a collector surface element; \mathbf{e}_0 is the unit vector connecting the particle center to the origin of the hemisphere collector; dS is the surface element from the collector surface and is related to particle surface element dA as $(\mathbf{n}_s \cdot \mathbf{e}_0) dS = (\mathbf{n}_A \cdot \mathbf{e}_0) dA$, where \mathbf{n}_s and \mathbf{n}_A are the normal unit vectors of surface elements dS and dA , respectively (Figure 2); and $p(h) (= F_{\text{EDL}}(h) + F_{\text{vdW}}(h))$ is the combined electric double layer and van der Waals interaction forces per unit area of the projected particle surface element dA onto the collector. This process is described in further detail in the Supporting Information. At a given separation distance h between any pair of the discretized collector and colloid surface elements, the interacting forces per unit area were approximated with a plate–plate configuration according to the following expressions:^{32,33}

$$F_{\text{EDL}}(h) = -\frac{\epsilon_0 \epsilon_r \kappa^2}{2} (\zeta_p^2 + \zeta_c^2) \left[\text{cosech}^2(\kappa h) - \frac{2\zeta_p \zeta_c}{\zeta_p^2 + \zeta_c^2} \text{cosech}(\kappa h) \coth(\kappa h) \right]$$

$$F_{\text{vdW}}(h) = -\frac{H}{6\pi h^3} \quad (2)$$

where ϵ_0 is the dielectric permittivity of vacuum, ϵ_r is the relative dielectric constant of the fluid, κ is the inverse Debye length, ζ_p and ζ_c are the respective zeta-potentials of the elements on the colloid and the heterogeneously charged collector surface, and H is the nonretarded Hamaker constant for the system (i.e., colloid–water–collector). Because the discretized surface elements together describe spherical surfaces, integration over both the colloid and collector surfaces in eq 1 with varied h values approximates sphere–sphere interaction system analogously to the Derjaguin approximation.

Following the Duffadar and Davis approach,^{22,23} the nonretarded van der Waals interactions were considered in the GSI force computation. For a given ionic strength (IS), the attraction calculated using the nonretarded van der Waals force is larger than that calculated using the expression with retardation. For qualitative demonstration of, for example, retention without attachment, a higher ionic strength may be required for the retarded relative to the nonretarded van der Waals expression. However, this difference is unimportant for our goal to demonstrate that these mechanisms occur in our simulations. In the GSI technique, the total colloid–surface interaction force (eq 1) was determined from the sum of

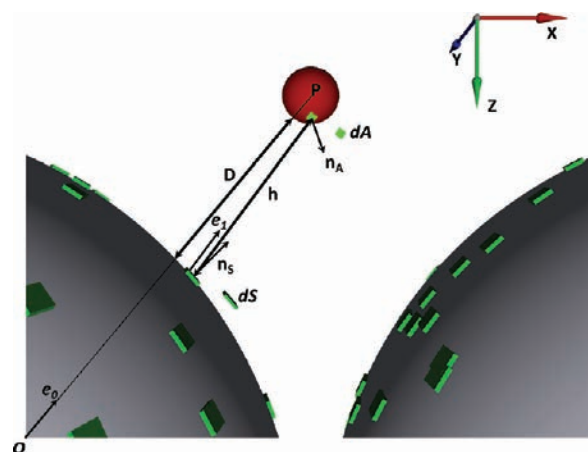


Figure 2. Schematic illustration of GSI discretization. The heterodomains over the hemisphere collector surfaces were depicted as little squares (black). Both colloid and collector surfaces were discretized into small surface elements of size same as those of the heterodomains. \mathbf{e}_0 is the unit vector connecting the particle center to the origin of the hemisphere collector, \mathbf{e}_1 is the unit vector that specifies the direction between an element on the colloidal particle surface (dA , e.g., the red square) and a collector surface element (dS , square in red or black), and dS is related to dA as $(\mathbf{n}_s \cdot \mathbf{e}_0) dS = (\mathbf{n}_A \cdot \mathbf{e}_0) dA$, where \mathbf{n}_s and \mathbf{n}_A are the normal unit vectors of surface elements dS and dA , respectively. D is the minimum separation distance between the colloid and the collector surfaces, and h is the local separation distance between a collector surface element and a colloid surface element.

the contributions from each surface element interaction with the elements on the other surface (eq 2), such that depending on the number of heterodomains present in the zone of interaction at any step of the trajectory, a continuum of net forces could exist between fully repulsive (no heterodomains present) and fully attractive (sufficient heterodomains present to yield a net attractive interaction). The modified GSI technique here for a sphere–sphere system is expected to produce similar predictions to the sphere–plate system of Duffadar and Davis,^{22,23} provided that the surface friction is allowed to extend to secondary energy minimum as done by the original authors (discussed further below).

Particle Trajectory Analysis. Trajectories of colloids within the hemispheres-in-cell model were mechanistically simulated based on classical Langevin equation

$$(m + m^*) \frac{du}{dt} = F_D + F_G + F_L + F_{\text{COLL}} + F_B \quad (3)$$

where m is the mass of the colloidal particle, m^* is the virtual mass (approximated by one-half of the displaced fluid volume by the colloid), and u is the particle velocity vector. On the right-hand of the above equation are forces acting on the colloidal particle, including fluid drag (F_D), gravity (F_G), shear lift (F_L), colloidal interaction forces (F_{COLL}) which include electrostatic (F_{EDL}) and van der Waals (F_{vdW}) interactions, and Brownian forces (F_B). Among the forces, F_L and F_{COLL} only act on the particle in the normal direction relative to the collector surface. The drag forces at distances close to the collector surface were corrected as a result of hydrodynamic retardation as described elsewhere.^{4,28} The expressions for the forces in eq 3 are provided in Appendix A, with the exception that the colloid–surface forces were calculated via two different techniques as described below. When colloid–surface interactions were significant (at separation distances less than or equal to those corresponding to secondary energy minimum interactions), they were computed using the GSI technique. Otherwise, mean-field interaction forces were calculated in order to reduce computational expense. At each simulation time step, the colloidal forces between a colloid and each of the hemisphere collector surfaces were computed.

An adaptive time-stepping strategy was used in integrating all the forces acting on the particle to obtain particle velocities according to the above equation, as described in our previous papers.^{4,27,28} At each time step, the integration was carried out in the normal and tangential direction relative to the collector surface respectively. The particle velocity vector (u_n , u_t) at time step τ was obtained from previous time step $\tau - 1$ as follows:²⁸

$$u_n^\tau = \frac{\left(m + \frac{2}{3}\pi a_p^3 \rho_f\right) u_n^{\tau-1} + (F_n^{\text{GRP}} + 6\pi\mu a_p v_n f_2) \Delta t}{\left(m + \frac{2}{3}\pi a_p^3 \rho_f + \frac{6\pi\mu a_p}{f_1} \Delta t\right)}$$

$$u_t^\tau = \frac{\left(m + \frac{2}{3}\pi a_p^3 \rho_f\right) u_t^{\tau-1} + \left(F_t^{\text{GRP}} + \frac{f_3}{f_4} 6\pi\mu a_p v_t\right) \Delta t}{m + \frac{2}{3}\pi a_p^3 \rho_f + \frac{1}{f_4} 6\pi\mu a_p \Delta t} \quad (4)$$

where a_p is the radius of the particle, $F_n^{\text{GRP}} = F_G^n + F_L + F_{\text{COLL}} + F_B^n$, and $F_t^{\text{GRP}} = F_G^t + F_B^t$; the superscript and subscript n and t refer to the normal and tangential direction with respect to the collector surface, respectively.

Upon resolving the particle velocity vector $u(u_n, u_t)$, the updated particle position was determined from first-order integration ($dx/dt = u$), where x is the particle position vector. Following the translation step, forces acting on the particle were determined, and the process was repeated until the particle reached the vicinity of the collector surface (at specified distance), where the additional forces and/or torques (e.g., friction force) were considered.

Incorporation of Friction Forces and Torques upon Contact. Following the treatment in Duffadar and Davis,^{22,23} we incorporated into the overall force balance equation the frictional forces caused from a moving colloid upon contact with the collector surface. However, the definition for “physical contact” between a moving colloid and the surface remains debated. Duffadar and Davis^{22,23} invoked frictional forces when colloid–surface interaction forces were attractive, which corresponds to both primary and secondary energy minima, similar to the approach used by Torkzaban et al.¹⁸ In this work, we considered surface frictional forces operational only when colloids were associated with the primary energy minimum. In other words, the term “upon contact” is used here to refer to the case where colloid–surface separation distances are less than or equal to that corresponding to the energy barrier maximum, as calculated from mean-field DLVO theory (absent discrete surface heterogeneities).

Two types of friction were considered: (i) dynamic frictional force (equal to $\mu_F F_n$, where μ_F is the dynamic friction coefficient and F_n represents all forces acting on the colloid normal to the collector surface), which determines whether the colloid slips or rolls along the surface; (ii) rolling friction force (equal to $\mu_R F_n$, where μ_R is the rolling friction coefficient, which depends upon the material properties of the surfaces in contact and is independent of the colloid velocity). The rolling friction determines whether the particle continues to roll or becomes immobilized by contact (by the elastic deformation of the surfaces in response to contact, as well as by imperfections that also give rise to rolling resistances).

Upon contact, the particle velocity in the tangential direction relative to the collector surface at time τ was related to that at previous time $\tau - 1$ as follows (see Supporting Information for more details and Appendix B for expressions on hydrodynamic retardation functions):

$$u_t^\tau = \left[u_t^{\tau-1} \left(m_p + \frac{2}{3}\pi a_p^3 \rho_f \right) + F_t^{\text{GRP},\tau} \Delta t + \mu_R^{\tau} F_n^{\tau} \Delta t \right. \\ \left. + 6\pi\mu a_p v_t^{\tau} \Delta t \left(F_t^{*s} + T_y^s \frac{2}{3} \frac{a_p}{h} \right) \right] / \left[\left(m_p + \frac{2}{3}\pi a_p^3 \rho_f \right) \right. \\ \left. - 6\pi\mu a_p \Delta t \left(F_t^{*r} + F_t^{*s} a_p + T_y^{*r} \frac{4}{3} + T_y^{*s} \frac{4}{3} a_p \right) \right] \quad (5)$$

Table 1. Parameters Used in Trajectory Simulations

symbol	parameter	simulation value
d_c	collector diameter	510 μm
ε	porosity	0.37
v_p	pore water velocity	4 m/day
d_p	colloid diameter	0.5, 10 μm
ρ_p	colloid density	1.055 g/cm ³
ρ_f	fluid density	0.998 g/cm ³
μ	fluid viscosity	9.98×10^{-4} kg/(m.s)
H	Hamaker constant	3.84×10^{-21} J
T	absolute temperature	298.2 K
IS	ionic strength	0.1–50 mM
ζ_p	colloid zeta potential	−40, −60 mV
ζ_c	collector zeta potential	−40, −20 mV
ζ_h	heterodomain zeta potential	5, 40, 60 mV
— — —	heterodomain size	10–400 nm

To illustrate the condition for immobilization, the above equation can be simplified by considering the steady-state conditions ($du_t/dt = 0$) and assuming that, within primary energy well, Brownian forces and gravity are insignificant (i.e., $F_t^{\text{GRP}} \approx 0$, F_n is the only external force acting):

$$u_t = \frac{-\frac{\mu_R F_n}{6\pi\mu a_p} - v_t \left(F_t^{*s} + T_y^s \frac{2}{3} \frac{a_p}{h} \right)}{\left(F_t^{*r} + F_t^{*s} a_p + T_y^{*r} \frac{4}{3} + T_y^{*s} \frac{4}{3} a_p \right)} \quad (6)$$

Immobilization occurs when rolling friction dominates the other terms and u_t is diminished to zero.

Attachment Criteria. For this study, the criteria for direct attachment of colloids onto the collector surface were either (1) <1 nm separation distance, where van der Waals attractions strongly dominate over electrostatic repulsions and result in colloid attachment, or (2) immobilization via eq 6.

Heterogeneous Domain Generation. Positively charged heterogeneous domains (heterodomains) were randomly generated and distributed over the spherical collector surfaces in the hemispheres-in-cell model. A random number generator was employed to obtain the center location of each heterodomain, and the generated heterodomains were rejected if they overlapped with previously generated ones. The total number of heterodomains varied according to specified heterodomain coverage and size, but was typically maintained at a few million to limit computational intensity. Minimization of numerical intensity in tracking heterodomains is described in the Supporting Information.

Simulation Parameters and Conditions. The simulations in this work were performed under conditions where mean field theory predicts unfavorable interactions, i.e., both colloid and collector surfaces were bulk negatively charged. Table 1 shows the parameters and conditions used in the trajectory simulations. The parameter values were selected to mimic the conditions typically used in our column experiments for investigating the retention behavior of different size polystyrene colloidal particles in a randomly packed bed of glass beads in ground-water flow regime under unfavorable conditions.^{3,34}

RESULTS AND DISCUSSION

Below, we present simulations of colloid retention under conditions spanning colloid–collector interactions from favorable to unfavorable. In mean-field theory, this span is accomplished by changing the parameters governing colloid–surface interaction, e.g., surface potentials and Hamaker constant, and the

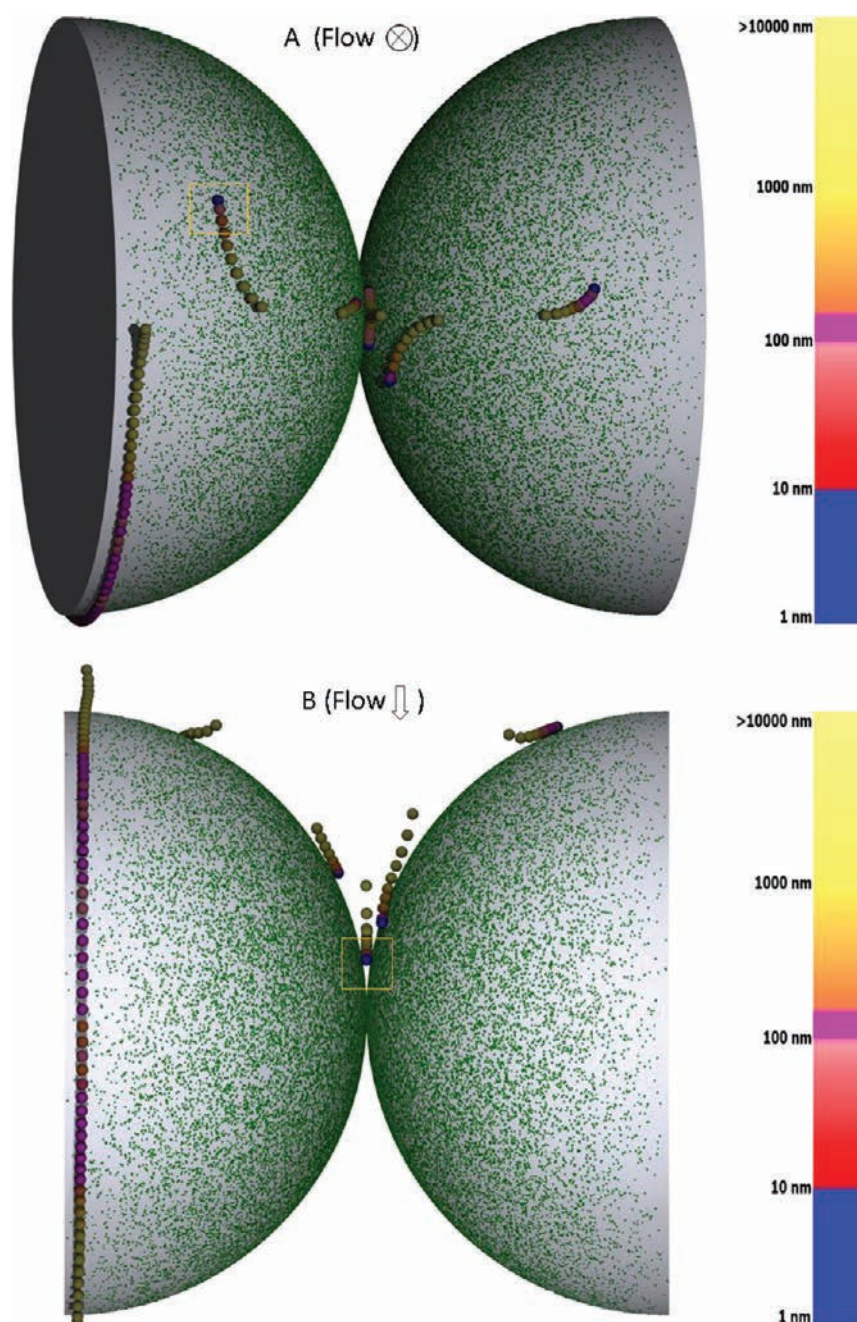


Figure 3. Images showing representative trajectories of retained or re-entrained $10\ \mu\text{m}$ diameter colloids simulated in the hemispheres-in-cell model (flow originating from top as shown in Figure 1) under a representative unfavorable condition with heterodomain coverage of 25%: A (top view) and B (side view). The zeta potentials for colloids, collector, and heterodomains are -60 , -20 , and $+60$ mV, respectively; heterodomain: size, 300 nm; number, 2.27 millions; ionic strength: 1 mM. Colloids are rendered in various colors based on the colloid–collector separation distances as indicated by the color spectrum, and distances corresponding to secondary and primary energy minimum are marked with magenta and blue, respectively. The heterodomains are shown as discrete green patches over the collector surfaces. The near-surface trajectories of the colloids highlighted in orange boxes were shown in Figures 4 and 5. See Table 1 for other parameter values.

parameters that represent the surfaces are spatially invariant. In the approach below, the interactions are governed by a combination of repulsion to “bare” surface and attraction to discrete heterodomains, such that the span from unfavorable to favorable conditions is accomplished by changing the surface coverage by heterodomains, which can be done by changing both their size and spatial frequency. We begin by demonstrating the influence of surface coverage on colloid retention, and on the mechanisms

of retention, for $10\ \mu\text{m}$ diameter colloids. This colloid size was used because it is capable of retention by all known mechanisms, whereas colloids smaller than $\sim 2\ \mu\text{m}$ in diameter are not expected to undergo wedging in grain-to-grain contacts according to both experiment³ and theory.⁴ We performed the simulations for representative unfavorable conditions using zeta potentials for the colloid, collector, and heterodomains equal to -60 , -20 , and $+60$ mV, respectively, at an ionic strength of 1 mM, and a

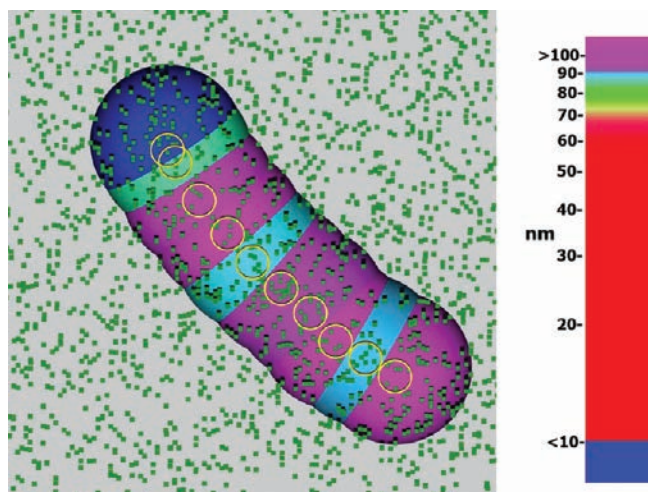


Figure 4. Image showing the near-surface trajectory locations (e.g., from secondary energy minimum toward the surface) for a colloid prior to its attachment on the open surface (highlighted in an orange box in Figure 3A). This figure is viewed from within the transparent collector outward toward the attaching colloid. The color of the colloid reflects the colloid–collector separation distances using a very detailed color spectrum, and distances corresponding to secondary and primary energy minimum are marked with magenta and blue, respectively. The heterodomains are shown in green and the zone of influence (ZOI) is highlighted with a yellow circle.

pore water velocity of 4 m/day (see Table 1 for other simulation conditions). For each simulation run, 1000 colloid trajectories (with randomly distributed initial locations) were simulated to obtain a statistically meaningful collector efficiency, which is defined as the ratio of the number of colloids being retained relative to the number of colloids introduced to the system. These conditions are not intended to be comprehensive, but demonstrate the ability of the hemispheres-in-cell model with heterogeneity to reproduce non-straining mechanisms of colloid retention under unfavorable conditions model. A comprehensive comparison to existing data is beyond the scope of this introduction, but is in development.

Trajectories, Final Locations, and Mechanisms of Retention. The trajectories of retained or re-entrained 10 μm colloids under unfavorable condition for 25% coverage by heterodomains (2.27 million 300 nm squares) in the hemispheres-in-cell model are shown in Figure 3 A (top view) and B (side view), where the color of the colloid indicates its separation distance from the collector surface. The final locations of retention from these trajectories included: (1) the open surface and (2) grain to grain contact. For both types of locations, the final separation distances were less than 4.5 nm, reflecting the two attachment criteria implemented here, i.e., either with separation distances ≤ 1 nm, or immobilization via eq 6 (with final separation distances of 1–4.5 nm). These final locations of attachment were within the primary energy well (marked by blue color), indicating genuine attachment to the surface, and suggesting that local reduction or elimination of repulsion via heterogeneity resulted in attachment at two environments: (1) the open surface; (2) grain to grain contacts. These mechanisms are further elucidated by simulated colloid trajectories (Figure 3A,B), which provide the near-surface movements of the colloids under unfavorable conditions prior to their retention. The reason we

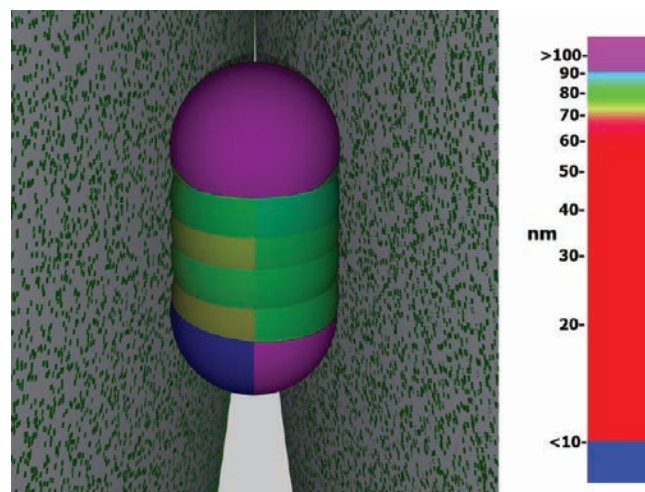


Figure 5. An image showing the near-surface trajectory for a colloid becoming wedged at the grain to grain contact (highlighted in an orange box in Figure 3B), where the colloid is split into two halves, with its colors indicating the corresponding separation distances to the two bonding collector surfaces. The distances corresponding to secondary and primary energy minimum are marked with magenta and blue, respectively. The heterodomains from two bonding surfaces are shown in green.

distinguish these environments is further explained below. These trajectories are also provided as a movie (Supporting Information).

The trajectories demonstrate that those colloids that were attached to the open surface translated across the collector surface at separation distances nominally corresponding to the mean-field secondary energy minimum (e.g., 90–120 nm) (shown in magenta) until finding a location where surface coverage by heterodomains was sufficient to locally reduce or eliminate repulsion. This is more evident in an enlarged image (Figure 4) showing each near-surface location between translations of a colloid (highlighted in the orange box in Figure 3A) immediately prior to attachment on the open surface (again, the color of the colloid indicates its separation distance). Figure 4 is viewed from within the transparent collector outward toward the attaching colloid. The heterodomains on the collector surface are shown in green, as are the heterodomains that are located within the zone of influence (ZOI) between the colloid and collector.²³ According to Duffadar and Davis,²³ the radius of the ZOI is proportional to $(\kappa^{-1} a_p)^{1/2}$, where κ^{-1} is the Debye length. The ZOI is shown by the yellow circle for each translation. The heterodomains within the ZOI contribute significantly to the overall colloid–surface interaction. However, in addition to the number of heterodomains within the ZOI, the spatial arrangement of heterodomains within the ZOI also influences the interaction force, since those closest to the center of the ZOI have the greatest influence due to curvature of the colloid and collector surfaces. Additionally, random fluctuation of the colloid in response to diffusion within the mean-field secondary energy minimum also influences the separation distance (Figure 4), such that attachment did not occur at points in the trajectory where many heterodomains were present in the ZOI because there happened to be greater colloid–surface separation at these locations. These translations are also provided in a movie in the Supporting Information.

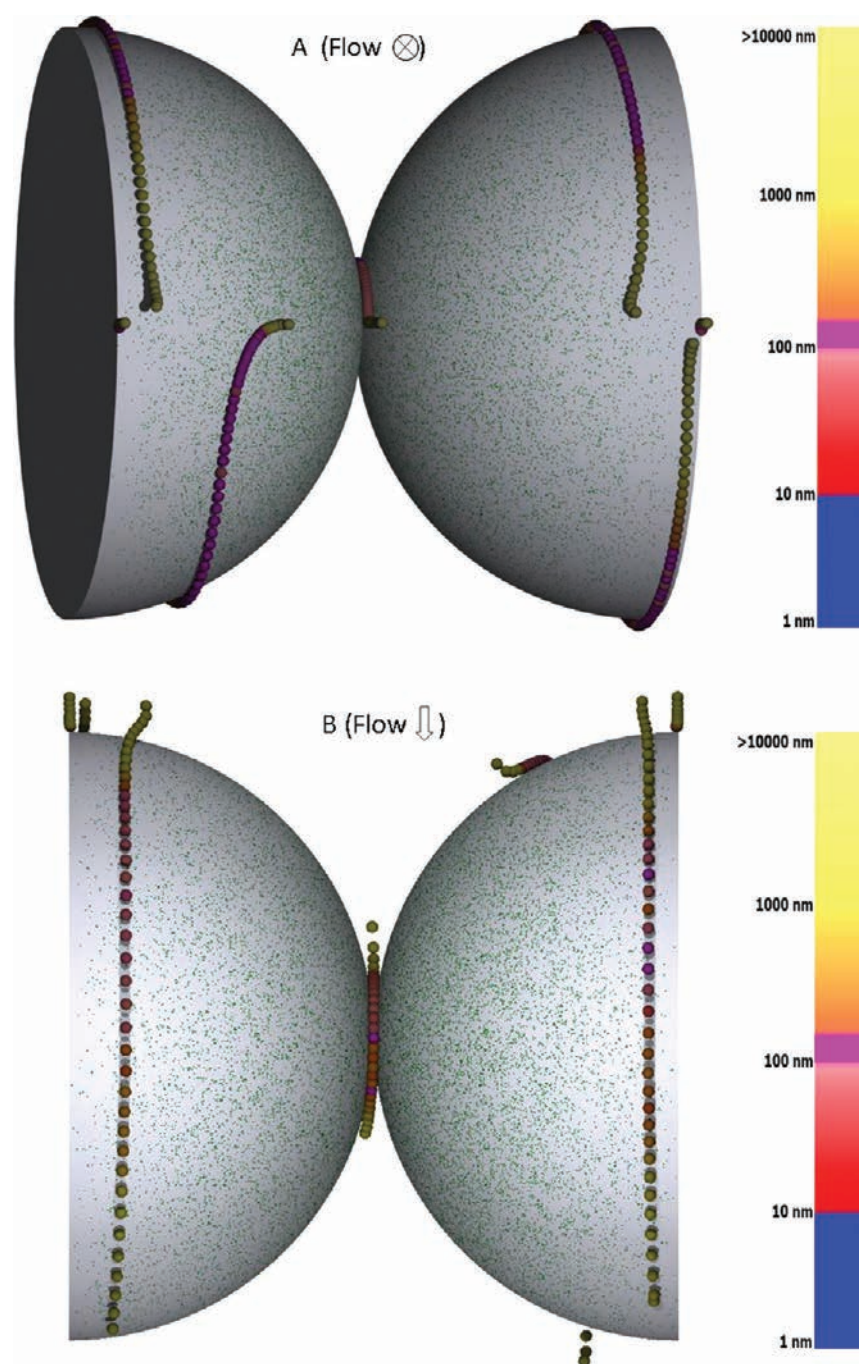


Figure 6. Images showing representative trajectories of retained or re-entrained 10 μm diameter colloids simulated in the hemispheres-in-cell model under unfavorable conditions with heterodomain coverage of 15%: A (top view) and B (side view). The zeta potentials for colloids, collector, and heterodomains are -60 , -20 , and $+60$ mV, respectively; heterodomain: size, 248 nm; number, 2 million; ionic strength: 1 mM. Colloids are rendered in various colors based on the colloid–collector separation distances as indicated by the color spectrum, and distances corresponding to secondary and primary energy minima are marked with magenta and blue, respectively. The heterodomains are shown as discrete green patches over the collector surfaces. See Table 1 for other parameter values.

The near-surface trajectory for a colloid wedged into the grain to grain contact (as highlighted in the orange box in Figure 3B) is shown in Figure 5, where the color of the colloid is split into two halves; the color on each half indicating the corresponding separation distance of that half to its bonding collector surface in the grain to grain contact. The trajectories show that the process of wedging was initiated by simultaneous association of the colloid with two adjacent collector surfaces, each at separation

distances corresponding to the mean-field secondary energy minimum (shown in magenta, Figure 5). The colloid translated along the two bonding surfaces in the grain to grain contact with fluctuating separation distances to the two bonding collectors until finding a location where surface coverage by heterodomains on one of the surfaces was sufficient to locally reduce or eliminate repulsion on one of the collector surfaces, where it attached to that surface while maintaining secondary energy minimum contact

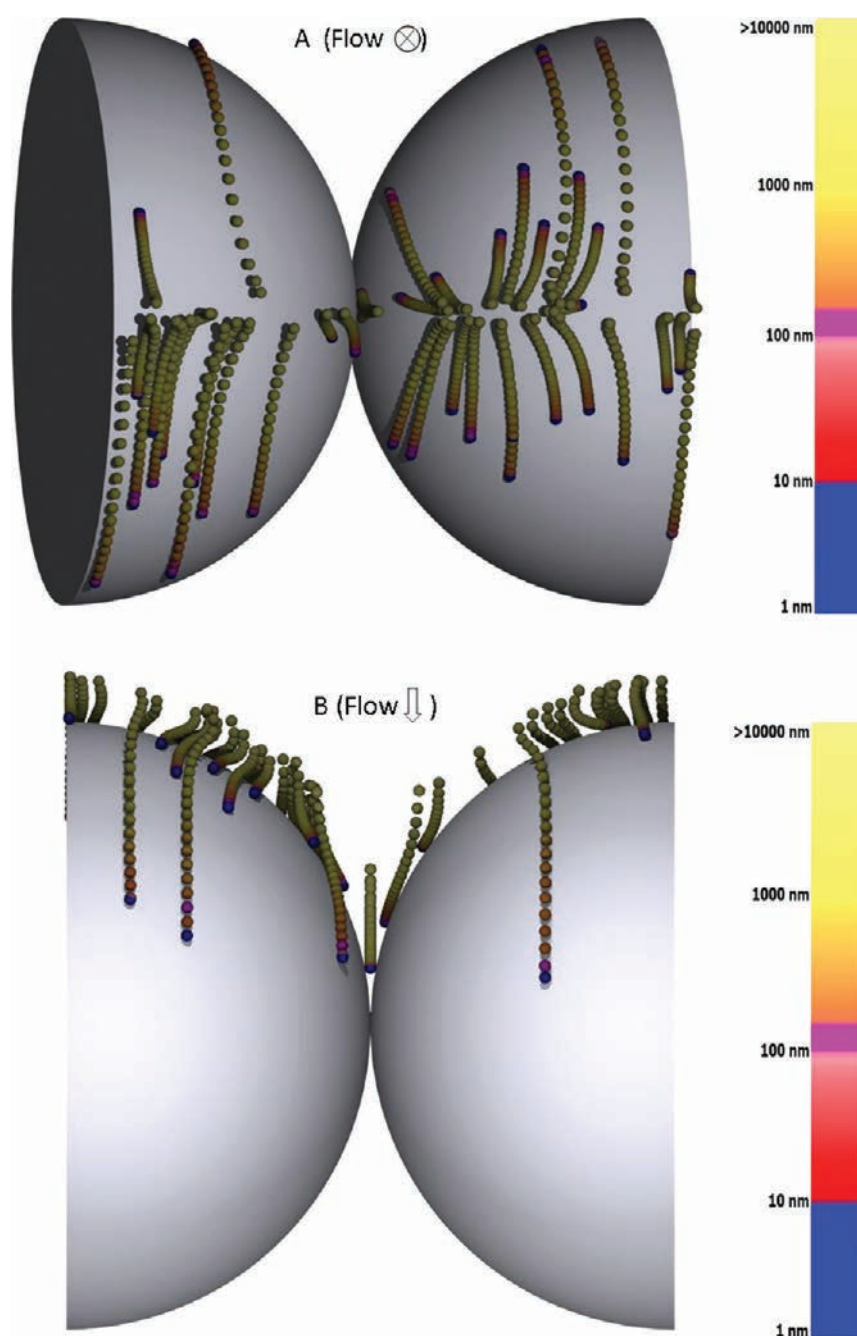


Figure 7. Images showing trajectories for retained 10 μm diameter colloids simulated in the hemispheres-in-cell model under favorable conditions: A (top view) and B (side view). Favorable condition was achieved by using the oppositely charged collectors versus colloids (e.g., ζ_p -60 mV; ζ_c $+20$ mV). Colloids are rendered in various colors reflecting the colloid–collector separation distances as indicated by the color spectrum, and distances corresponding to secondary and primary energy minimum are marked with magenta and blue, respectively. See Table 1 for other parameter values.

with the second surface (Figure 5). A plot showing the changes in separation distances of this colloid to the two bounding surfaces is provided in the Supporting Information. An image analogous to Figure 4 showing the near-surface locations with zones of influence for this wedged colloid is also provided in the Supporting Information. Examination of trajectory data reveals that the averaged fluid velocities at the colloid center are reduced (by about 50–70%) in the proximity of two bonding surfaces (e.g., grain to grain contact region) versus a single surface (i.e., the open surface) for equivalent flow fields, because the colloid is found to be approximately

15–25 nm closer to the surface for the two-surface case (for the conditions simulated here), and also because the fluid velocities proximal to two bonding surfaces are lower for a given separation distance relative to the single-surface case due to the no-slip boundary conditions for the fluid at the surfaces. Secondary minimum association with two bonding surfaces helps to bring the colloid slightly closer to the surface, but cannot arrest the colloid. The simultaneous bonding by two energy barriers does allow the colloid to push slightly into the energy barrier; however, the colloid overcomes only approximately 5% of the overall energy barrier

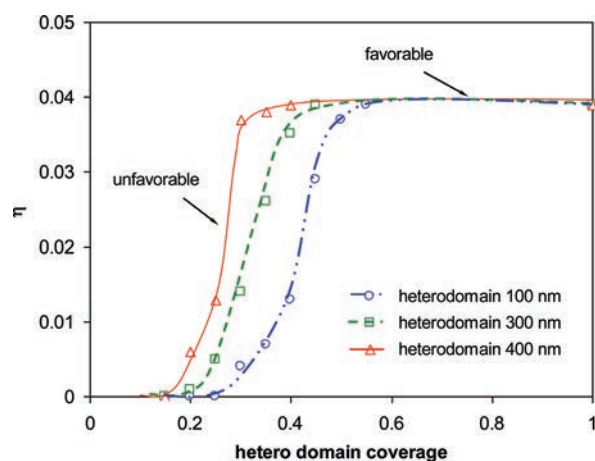


Figure 8. Simulated collector efficiencies (η) for 10- μ m-diameter colloids under unfavorable conditions in response to the change in the coverage and size of positively charged heterodomains. Zeta potentials for colloids, collector, and heterodomains are -60 , -20 , and $+60$ mV, respectively; ionic strength, 1 mM; representative heterodomain sizes: 100, 300, 400 nm. See Table 1 for other parameter values. The lines were drawn to reflect the trends displayed from the discrete simulation data.

under the conditions shown here. The likelihood of attachment in the grain-to-grain contact is increased not only by the reduced fluid velocity in the area bound by two surfaces, but also by doubling the likelihood of finding sufficient heterodomains to reduce or eliminate colloid-surface repulsion. It should be noted that a previous report⁴ that simulated colloid attachment in the grain-to-grain contact in the absence of heterogeneity (for energy barriers greater than approximately 10 kT) was incorrect due to a single error in the code concerning coordinate transformation. However, direct experimental observation³ demonstrates the occurrence of colloid retention on both the open surface and, for colloids larger than approximately 2 μ m, the grain to grain contact, both of which are captured in these simulations that include surface charge heterogeneity.

The trajectories of retained or re-entrained 10 μ m colloids under unfavorable condition for 15% surface coverage by heterodomains (2 million 248-nm squares) show that there was no direct attachment to the collector surface (Figure 6A and B) since the separation distances of their final locations were all well above 10 nm. Instead, some colloids were retained at the forward flow stagnation zones with final separation distances of ~ 90 –120 nm, corresponding to the mean-field secondary energy minimum. The portion of the trajectory that resided in the flow stagnation zone accounted for more than 20 s, demonstrating that these colloids were not immobilized, but rather were retained without attachment. The average duration of the trajectories that show colloids skimming along the collector surfaces prior to re-entrainment (Figures 6A,B and 3B) were approximately 45 s. Since these retained colloids were associated with the secondary energy minimum, they would be released if subject to solution ionic strength reduction or pH change to eliminate the secondary minimum, which could partially explain the observed reversible retention (typically only a small fraction of total retained colloids) from experiments.^{15,35} The contrasting mechanisms of retention between the 25% and 15% surface coverages (attachment on open surface and grain to grain contacts versus retention without attachment, respectively) demonstrates the influence of heterodomain surface coverage on the extent and mechanism of retention.

Specifically, at low heterodomain coverage, retention did not occur by direct attachment, but instead by retention without attachment via secondary energy minimum association in a zone of low fluid drag.

The colloid trajectories simulated for 25% and 15% coverages by heterodomains (Figures 3 and 6) demonstrate protracted translation along the surface at distances corresponding to the mean-field secondary energy minimum. The stochastic nature of the process is demonstrated by some of the near-surface colloids becoming attached to the collector surface (e.g., Figures 3A,B, 4, and 5), or being retained at flow stagnation zones without attachment (e.g., Figure 6A,B), whereas other near-surface colloids were re-entrained back into the bulk flow (e.g., Figures 3B and 6A,B).

In contrast to both of the above surface coverages under unfavorable conditions, simulations under favorable conditions (collector surface zeta potential = $+20$ mV) did not show significant translation of colloids along the collector surface outboard of the energy barrier (Figure 7A and B), as seen by the lack of magenta in the trajectories, which corresponds to the mean-field secondary energy minimum. The trajectories are yellow (separation distances much greater than the mean-field secondary energy minimum) except for the last few translations that lead directly to the primary energy minimum (blue) attachment. Notably, the duration of these favorable condition trajectories were typically less than 10 s. The contrasting behaviors and mechanisms simulated between favorable and unfavorable conditions agree well with experimental observations.³ Furthermore, the three non-straining mechanisms of retention under unfavorable conditions that have been well-supported by experiments³ (local reduction of repulsion via surface heterogeneity, wedging in grain-to-grain contacts, and retention of secondary energy minimum-associated colloids in zones of low fluid drag) are reproduced by the simulations.

Retention versus Heterodomain Size and Surface Coverage. Between the extremes of retention corresponding to strongly unfavorable conditions (zero retention) and retention corresponding to favorable conditions (maximum retention), there exists a continuum of collector efficiencies (η) that vary according to heterodomain size and surface coverage (Figure 8). For a specific simulated heterodomain size, the total number of the heterodomains was varied to yield the overall heterodomain surface coverage as shown in Figure 8. Changes in η versus heterodomain coverage for three representative heterodomain sizes for 10 μ m colloids are shown for the following conditions (ζ_p -60 mV; ζ_c -20 mV; IS 1 mM; and ζ_h $+60$ mV).

Regardless of heterodomain size, no colloid attachment was observed below a surface coverage threshold in the range 10–20% (Figure 8). Above this threshold, simulated η increased with increasing heterodomain surface coverage (under otherwise equivalent conditions), demonstrating the influence of heterodomains on colloid-surface-flow interaction. At surface coverages greater than approximately 35–55%, simulated η s corresponded to favorable conditions for deposition. The mechanisms of retention also varied across this span. Under low surface coverage (e.g., $<25\%$), colloids were primarily retained in flow stagnation zones (e.g., as shown in Figure 6), or were wedged at the grain-to-grain contact (e.g., as shown in Figure 3); whereas for higher heterodomain coverage (e.g., >25 –30%), colloids were mainly attached on the open surface of collectors (e.g., as shown in Figure 3).

Notably, for a given surface coverage, larger heterodomain sizes resulted in greater colloid retention (higher η) relative to smaller

heterodomain sizes, despite the latter having higher spatial frequency (Figure 8). Likewise, smaller heterodomain sizes require greater surface coverage to achieve retention corresponding to favorable conditions (Figure 8). These simulations conform to simulations and experimental results for colloid attachment on heterogeneous planar surfaces in simple shear flow,^{36,37} where the authors also observed similar influence of heterogeneous patches on colloidal retention using various density (and/or size) of the patches.

Effect of Ionic Strength, Colloid Size, and Heterodomain Zeta Potential on Retention. The progression of colloid retention from high (favorable) to low (unfavorable) can also be realized via changing the solution ionic strength (IS). Figure 9a shows that the simulated collector efficiency (η) increased with increasing ionic strength, as expected, due to compression of the repulsive electric double layer interactions. This is shown for two colloid/heterodomain sizes (10 μm /100 and 500 nm/50 nm) and a fixed surface coverage by heterodomains (20%). Zeta potentials for the colloid, collector, and heterodomains were -40 mV, -40 mV, and $+40$ mV, respectively. The mean-field DLVO interaction energy profiles for these two colloid sizes at various ionic strengths investigated are provided in the Supporting Information for comparison.

At IS values greater than approximately 30 mM for the 10 μm colloids and 1 mM for the 500 nm colloids, η corresponded to those values expected under favorable conditions (0.04 and 0.015 for the 10 μm and 500 nm colloid, respectively).²⁸ At IS values below these thresholds, the simulated η values gradually decreased with decreased ionic strength (Figure 9a), a phenomenon that has not been captured in mean-field simulations.

The contrasting threshold ionic strengths to achieve favorable colloid-surface interactions for the 500-nm versus the 10- μm colloids (1 mM versus 30 mM, respectively), reflects the lower repulsive energy barriers experienced by smaller colloids under otherwise equivalent conditions. Notably, attachment of 500-nm colloids occurred for surface coverage by heterodomains as low as $\sim 5\%$ (at 1 mM) (data not shown), in agreement with Duffadar et al.,³⁶ who reported that the threshold heterodomain coverage necessary to allow attachment of submicrometer colloids was approximately 2%, far lower than that required for larger colloids.

Across the ionic strength range examined, the mechanisms of retention also varied. At low ionic strength (e.g., <10 mM), the 10 μm colloids were predominately wedged in grain to grain contact, or were retained at flow stagnation zones, whereas at high IS (e.g., >20 mM), these colloids were primarily attached to the open surface. In contrast, the environment of retention for the 500 nm colloids was predominately attachment at the open surface for all ionic strengths examined (e.g., 0.1–50 mM). Wedging in the grain to grain contact was not observed for these submicrometer colloids, and retention at flow stagnation zones via association with secondary energy minimum was minor.

Figure 9a also reveals that, at ionic strength between 1 and 30 mM, the collector surfaces were favorable for attachment of 500 nm colloids, but were unfavorable for attachment of 10 μm colloids, which required grain to grain contact conditions to be retained (wedged), i.e., interactions with two bounding surfaces and reduced fluid drag. This aspect of the simulations is also in agreement with direct experimental observations in packed glass beads under unfavorable conditions,³ where colloids less than 2 μm in diameter attached primarily on the collector open surface, whereas colloids greater than 2 μm in diameter were primarily retained in grain to grain contacts.

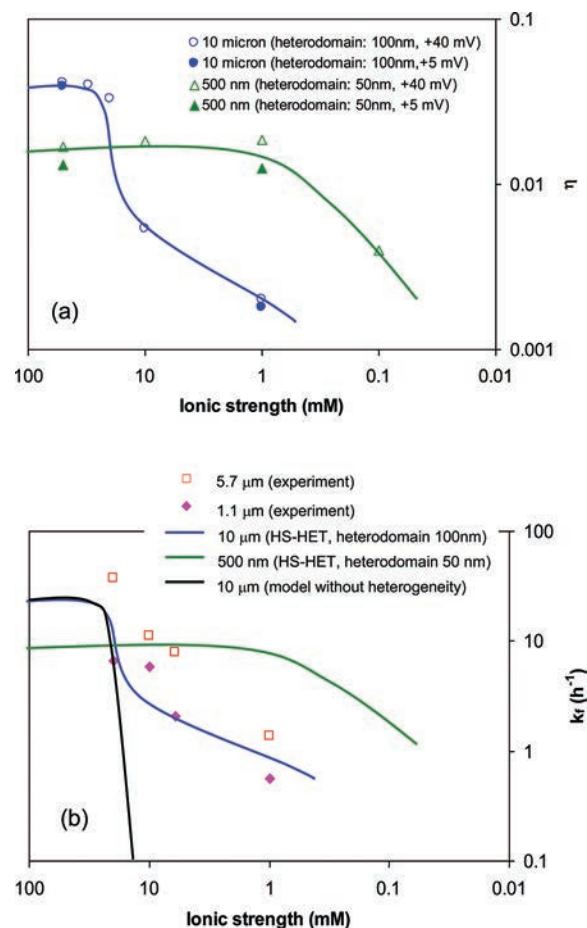


Figure 9. (a) Simulated collector efficiencies (η) under unfavorable conditions as a function of ionic strength and heterodomain zeta potentials for two representative colloid/heterodomain sizes (10 μm /100 nm and 500 nm/50 nm). The heterodomain coverage was 20%. The lines were drawn to reflect the trends displayed from the discrete simulation data. (b) Simulation results from (a) were converted to deposition rate constants (k_d), with only trend lines shown, to compare with predictions from model without heterogeneity and experimental data, which are taken from Johnson et al.³⁴ who conducted column experiments to investigate the retention behavior of the 5.7 and 1.1 μm colloids under a range of ionic strength and fluid velocity under unfavorable conditions.

Retention was relatively insensitive to the specific value of the heterodomain zeta potential (Figure 9a), where variation in heterodomain zeta-potential from $+40$ to $+5$ mV yielded similar values of η , and this was true for both the 10 μm and 500 nm colloids under otherwise equivalent conditions. As is true for mean-field favorable conditions, the simulations involving discrete heterodomains were relatively insensitive to the specific value of the favorable zeta potential. The lack of an energy barrier is primary, such that, as long as the energy barrier is absent, the rate of colloid interception with the surface is limited by transport to the surface rather than DLVO interactions.

Comparison to Experimental Data. The inability of mean-field simulations to capture experimentally observed trends in colloid retention as a function of ionic strength is well-known.^{31,35,38} Here, we show that the hemispheres-in-cell model with surface heterogeneity produces experimentally observed trends.

In Figure 9b, η was converted into a deposition rate coefficient (k_f) (details provided in the Supporting Information), which is independent of any specific model geometries to represent granular porous media. Values of k_f are shown as a function of solution ionic strength (IS) for both discrete heterodomain and mean-field theoretical predictions.

For mean field theory, an abrupt transition is observed from deposition corresponding to favorable conditions to zero deposition (Figure 9b). In contrast, and as originally pointed out for porous media by Elimelech and O'Melia,¹¹ experimentally observed deposition rate coefficients decrease much more gradually in response to IS reduction.^{31,35,38} This is shown in Figure 9b using data obtained for two colloid sizes (5.7 and 1.1 μm in diameter) under unfavorable conditions.³⁴ The predicted trend in deposition rate coefficients from the hemispheres-in-cell model with incorporation of surface heterogeneity qualitatively captures the experimental trend (Figure 9b). The discrepancies between simulated and observed retention in Figure 9b resulted from many factors; e.g., our simulation conditions may not exactly reflect the experiment conditions; in particular, the size and frequency of the heterodomains employed in the simulations may not adequately characterize the medium grain surface heterogeneity in the experiments. However, the sensitivity of our simulated retention trend to ionic strength and to heterodomain size and spatial frequency holds promise that these attributes can be backed out from unknown surfaces via comparison of experimental values of k_f to simulations, in order to allow a priori prediction of colloid retention in porous media. Future work will develop the quantitative relationships to allow prediction of colloid retention under unfavorable conditions.

Topographical Roughness and Colloid Surface Heterogeneity. In this work, we did not explicitly account for the topographical roughness of the surfaces; rather, we assume that, at the nanoscale, roughness and surface charge heterogeneities can both be represented by attractive heterodomains, since they both act to decrease the total interaction energy as well as the height of the energy barrier.³⁹ Hence, the underlying mechanisms of retention resulting from surface roughness may not be significantly dissimilar to those from surface charge heterogeneities considered here. Very recently, Bendersky and Davis⁴⁰ extended the GSI technique to compute the interactions between colloids and both chemically and topographically planar heterogeneous collector surfaces. Thus, we can accordingly modify our adapted GSI technique to explicitly account for the topographical roughness in the near future. Although the current work only considered heterogeneities on the collector surfaces, the GSI method can be easily implemented to account for the heterogeneities (charge or roughness) from the colloid surfaces as well, which will be directly related to study the transport and retention behavior of biological colloids such as bacteria.

SUMMARY

In this work, we have demonstrated that the hemispheres-in-cell model with consideration of surface heterogeneity is capable of producing all observed non-straining retention mechanisms in porous media under unfavorable conditions via mechanistic simulation of particle trajectories based on force and torque balances. The occurrence of these mechanisms is shown to depend upon the coupled colloid–collector–flow interactions, which themselves depend on factors such as the size and surface properties of colloids and collectors, the solution chemistry, and the flow field.

Simulated colloid retention behaviors under unfavorable conditions qualitatively agree with experimental observations, and our next goal is to characterize medium-grain surface heterogeneities so as to quantitatively predict retention of colloids in porous media.

APPENDIX

A. Expressions for Forces Used in Trajectory Simulations.

Below is a brief summary of forces that were considered in our particle trajectory simulations. The superscript and subscript n and t refer to the normal and tangential direction to the collector surface, respectively.

Shear lift force:^{41,42}

$$F_L = \frac{6.46\mu a_p^3 (\partial v / \partial r)^{3/2}}{(\mu/\rho)^{0.5}}$$

Mean-field electrostatic double layer force:³²

$$F_{EDL} = 4\pi\epsilon_r\epsilon_0\kappa a_p\zeta_p\zeta_c \left[\frac{\exp(-\kappa h)}{1 + \exp(-\kappa h)} - \frac{(\zeta_p - \zeta_c)^2}{2\zeta_p\zeta_c} \frac{\exp(-2\kappa h)}{1 - \exp(-2\kappa h)} \right]$$

The mean-field van der Waals interaction forces were approximated with a sphere-plate configuration since the collector size was much greater than the colloid sizes considered.³³

$$F_{vdW} = -\frac{Ha_p \lambda (\lambda + 22.232h)}{6h^2 (\lambda + 11.116h)^2}$$

Brownian forces:^{43–45}

$$F_B = R \sqrt{\frac{2\xi kT}{\Delta t}}$$

Drag force in the normal direction after corrected for hydrodynamic retardation:^{46,47}

$$F_D^n = -\frac{6\pi\mu a_p u_n}{f_1} + 6\pi\mu a_p v_n f_2$$

Drag force in the tangential direction is corrected for hydrodynamic retardation effect based on the force and torque balance:^{48–51}

$$F_D^t = -\frac{6\pi\mu a_p u_t}{f_4} + \frac{f_3}{f_4} 6\pi\mu a_p v_t$$

The universal hydrodynamic functions are approximated by the following expressions:⁴

$$f_1(\bar{h}) = 1.00 - 0.443\exp(-1.299\bar{h}) - 0.5568\exp(-0.32\bar{h}^{0.75})$$

$$f_2(\bar{h}) = 1.00 + 1.455\exp(-1.2596\bar{h}) + 0.7951\exp(-0.56\bar{h}^{0.50})$$

$$f_3(\bar{h}) = 1.00 - 0.5\exp(-2.5\bar{h}) - 0.3\exp(-20.0\bar{h}^{0.50})$$

$$f_4(\bar{h}) = 1.00 - 0.42\exp(-0.35\bar{h}) - 0.4\exp(-10.0\bar{h}^{0.8})$$

B. Expressions for Hydrodynamic Shear Force, Torque and Hydrodynamic Retardation Functions Used "Upon Contact".^{22,23}

$$F_t^{S*} = \frac{1.70073337 + 1.0221606(D/a_p)}{1 + 1.0458291(D/a_p) - 0.0014884706(D/a_p)^2}$$

$$T_y^{S*} = 0.054651334(18.276952 - \exp(-1.422943(D/a_p)))$$

$$F_t^{tr*} = -\frac{1}{0.14116 + 0.5967(D/a_p)^{0.2984}}$$

$$F_t^{r*} = \frac{0.05826 - 0.06126(D/a_p)^{0.557}}{0.0681 + (D/a_p)^{0.557}}$$

$$T_y^{tr*} = \frac{0.04362 - 0.0459(D/a_p)^{0.557}}{0.06801 + (D/a_p)^{0.557}}$$

$$T_y^{r*} = -\frac{0.312373 + 0.739(D/a_p)^{0.4906}}{0.0954 + (D/a_p)^{0.4906}}$$

■ ASSOCIATED CONTENT

S Supporting Information. Additional information on surface discretization in GSI technique, heterogeneous domain generation, surface friction forces upon contact, and mean-field DLVO interaction. This material is available free of charge via the Internet at <http://pubs.acs.org>.

■ AUTHOR INFORMATION

Corresponding Author

*Corresponding author. Email: william.johnson@utah.edu; Tel: (801)585-5033; Fax: (801)581-7065.

■ ACKNOWLEDGMENT

This article is based upon work supported by the National Science Foundation Chemical, Biological, and Environmental Transport and Hydrologic Science Programs (0822102) and the ACS PRF grant (50790-ND8). Any opinions, findings, and conclusions or recommendations expressed in this material are those of the authors and do not necessarily reflect the views of the National Science Foundation or the ACS PRF agency. We are grateful for the technical and facility support provided at the Center for High Performance Computing at the University of Utah. We also thank the four anonymous reviewers for their many constructive comments that greatly helped to improve this article.

■ NOMENCLATURE

a_c	collector radius (μm)
a_p	colloid radius (μm)
b	radius of fluid shell (μm) (Figure 1)
d_c	collector diameter (μm)
d_p	colloid diameter (μm)
D	the minimum separation distance (m) (Figure 2)
dA	surface area element from the colloid (m^2)
dS	surface area element from the collector surface (m^2)
\mathbf{e}_1	unit vector connecting collector-colloid surface area elements (Figure 2)
\mathbf{e}_0	unit vector connecting colloid center to hemisphere origin (Figure 2)
f_1, f_2, f_3, f_4	universal hydrodynamic functions (unitless)

F_B	Brownian force (N)
F_D	drag force (N)
F_{EDL}	electric double layer force (or force density) (N or N/m^2)
F_{vdW}	van der Waals force (or force density) (N or N/m^2)
F_{COLL}	colloid-collector interaction forces (N)
F_G	gravity $= 4\pi a_p^3(\rho_p - \rho_f)g/3$ (N)
F_L	shear lift force (N)
F_n^{GRP}	grouped normal force $= F_G^n + F_L + F_{COLL} + F_B^n$ (N)
F_t^{GRP}	grouped tangential force $= F_G^t + F_B^t$ (N)
F_t^{S*}	dimensionless hydrodynamic shear force
$F_t^{tr*}, F_t^{r*}, T_y^{tr*}, T_y^{r*}$	hydrodynamic retardation functions (unitless)
g	gravitational constant ($\text{N m}^2/\text{kg}^2$)
h	colloid – surface separation distance (m)
\bar{h}	dimensionless separation distance $= h/a_p$
H	Hamaker constant $= 3.84 \times 10^{-21}$ J
IS	ionic strength (mM)
k	Boltzmann constant $= 1.381 \times 10^{-23}$ J/K
k_f	deposition rate constant (h^{-1})
m	colloidal particle mass (kg)
m^*	virtual mass of particle (kg)
\mathbf{n}_A	normal unit vector of a colloid surface element (Figure 2)
\mathbf{n}_S	normal unit vector of a collector surface element (Figure 2)
R	Gaussian random number
T	absolute temperature (K)
T_y^{S*}	dimensionless hydrodynamic torque
\mathbf{u}	particle velocity vector (m/s)
\mathbf{x}	particle position vector (m)
\mathbf{v}	fluid velocity vector (m/s)
v_p	average pore water velocity (m/day)

■ GREEK LETTERS

Δt	time step (s)
ε	porosity
$\varepsilon_r \varepsilon_0$	permittivity of water $= 7.083 \times 10^{-10}$ $\text{C}^2/(\text{Jm})$
η	collector efficiency
κ	reciprocal Debye length (1/m)
λ	characteristic wavelength of interaction $= 1.0 \times 10^{-7}$ m
μ	dynamic viscosity of the fluid ($\text{kg}/(\text{m s})$)
μ_F	dynamic friction coefficient (dimensionless)
μ_R	rolling friction coefficient (dimensionless)
ρ_f	density of the fluid (kg/m^3)
ρ_p	density of the particle (kg/m^3)
ζ_p	zeta potential of the particle (mV)
ζ_c	zeta potential of the collector (mV)
ζ_h	zeta potential of heterodomains (mV)
τ	time in simulation (s)
ξ	friction coefficient $= \frac{6\pi\mu a_p}{f_1}$ (normal) and $\frac{6\pi\mu a_p}{f_4}$ (tangential) (kg/s)

■ REFERENCES

- (1) Yao, K.-M.; Habibi, M. T.; O'Melia, C. R. *Environ. Sci. Technol.* **1971**, 5 (11), 1105–1112.
- (2) Rajagopalan, R.; Tien, C. *AIChE J.* **1976**, 22 (3), 523–533.

- (3) Johnson, W. P.; Pazmino, E.; Ma, H. *Water Res.* **2010**, *44* (4), 1158–1169.
- (4) Johnson, W. P.; Li, X.; Yal, G. *Environ. Sci. Technol.* **2007**, *41* (4), 1279–1287.
- (5) Bradford, S. A.; Torkzaban, S.; Leij, F.; imunek, J.; Van Genuchten, M. T. *Water Resour. Res.* **2009**, *45* (2), W02414.
- (6) Elimelech, M. *Water Res.* **1992**, *26* (1), 1–8.
- (7) Bai, R. B.; Tien, C. J. *Colloid Interface Sci.* **1999**, *218* (2), 488–499.
- (8) Tien, C.; Ramarao, B. V. *Granular Filtration of Aerosols and Hydrosols*; Elsevier: Oxford, U.K. 2007.
- (9) Chang, Y. I.; Cheng, W. Y.; Chan, H. C. *Sep. Purific. Technol.* **2009**, *65* (3), 248–250.
- (10) Chang, Y.-I.; Chan, H.-C. *AIChE J.* **2008**, *54* (5), 1235–1253.
- (11) Elimelech, M.; O'Melia, C. R. *Environ. Sci. Technol.* **1990**, *24* (10), 1528–1536.
- (12) Shellenberger, K.; Logan, B. E. *Environ. Sci. Technol.* **2002**, *36* (2), 184–189.
- (13) Li, X.; Lin, C.-L.; Miller, I. D.; Johnson, W. P. *Environ. Sci. Technol.* **2006**, *40* (12), 3762–3768.
- (14) Bradford, S. A.; Simunek, J.; Bettahar, M.; Van Genuchten, M. T.; Yates, S. R. *Water Resour. Res.* **2006**, *42* (12), W12S15.
- (15) Hahn, M. W.; O'Melia, C. R. *Environ. Sci. Technol.* **2004**, *38* (1), 210–220.
- (16) Kuznar, Z. A.; Elimelech, M. *Colloids Surfaces A: Physicochem. Eng. Aspects* **2007**, *294* (1–3), 156–162.
- (17) Herzig, J. P.; Leclerc, D. M.; Legoff, P. *Ind. Eng. Chem.* **1970**, *62* (5), 8–35.
- (18) Torkzaban, S.; Bradford, S. A.; Walker, S. L. *Langmuir* **2007**, *23* (19), 9652–9660.
- (19) Torkzaban, S.; Tazehkand, S. S.; Walker, S. L.; Bradford, S. A. *Water Resour. Res.* **2008**, *44* (4), W04403.
- (20) Li, X.; Li, Z.; Zhang, D. *Environ. Sci. Technol.* **2010**, *44* (13), 4936–4942.
- (21) Johnson, W. P.; Tong, M. *Environ. Sci. Technol.* **2006**, *40* (16), 5015–5021.
- (22) Duffadar, R. D.; Davis, J. M. *J. Colloid Interface Sci.* **2007**, *308* (1), 20–29.
- (23) Duffadar, R. D.; Davis, J. M. *J. Colloid Interface Sci.* **2008**, *326* (1), 18–27.
- (24) Rizwan, T.; Bhattacharjee, S. *Langmuir* **2009**, *25* (9), 4907–4918.
- (25) Chrysikopoulos, C. V.; Abdel-Salam, A. *Colloids Surfaces A: Physicochem. Eng. Aspects* **1997**, *121* (2–3), 189–202.
- (26) Kemps, J. A. L.; Bhattacharjee, S. *Langmuir* **2009**, *25* (12), 6887–6897.
- (27) Ma, H.; Johnson, W. P. *Langmuir* **2010**, *26* (3), 1680–1687.
- (28) Ma, H.; Pedel, J.; Fife, P.; Johnson, W. P. *Environ. Sci. Technol.* **2009**, *43* (22), 8573–8579.
- (29) Long, W.; Hilpert, M. *Environ. Sci. Technol.* **2009**, *43* (12), 4419–4424.
- (30) Cushing, R. S.; Lawler, D. F. *Environ. Sci. Technol.* **1998**, *32* (23), 3793–3801.
- (31) Song, L.; Johnson, P. R.; Elimelech, M. *Environ. Sci. Technol.* **1994**, *28* (6), 1164–1164.
- (32) Hogg, R.; Healy, T. W.; Fuerstenau, D. W. *Trans. Faraday Soc.* **1966**, *62*, 1638–1651.
- (33) Elimelech, M.; Gregory, J.; Jia, X.; Williams, R. A., *Particle Deposition and Aggregation: Measurement, Modeling and Simulation*. Butterworth-Heinemann: Boston, 1995.
- (34) Johnson, W. P.; Tong, M.; Li, X. *Water Resour. Res.* **2007**, *43* (12).
- (35) Shen, C.; Li, B.; Huang, Y.; Jin, Y. *Environ. Sci. Technol.* **2007**, *41* (20), 6976–6982.
- (36) Duffadar, R.; Kalasin, S.; Davis, J. M.; Santore, M. M. *J. Colloid Interface Sci.* **2009**, *337* (2), 396–407.
- (37) Kalasin, S.; Santore, M. M. *Langmuir* **2008**, *24* (9), 4435–4438.
- (38) Johnson, W. P.; Li, X.; Assemi, S. *Adv. Water Resour.* **2007**, *30* (6–7), 1432–1454.
- (39) Suresh, L.; Walz, J. Y. *J. Colloid Interface Sci.* **1996**, *183* (1), 199–199.
- (40) Bendersky, M.; Davis, J. M. *J. Colloid Interface Sci.* **2011**, *353* (1), 87–97.
- (41) Saffman, P. G. *J. Fluid Mech.* **1965**, *22* (2), 385–400.
- (42) Saffman, P. G. *J. Fluid Mech.* **1968**, *31*, 624.
- (43) Kubo, R. *Rep. Prog. Phys.* **1966**, *29*, 255–284.
- (44) Li, A.; Ahmadi, G. *Aero. Sci. Technol.* **1992**, *16* (4), 209–226.
- (45) Ounis, H.; Ahmadi, G.; McLaughlin, J. B. *J. Colloid Interface Sci.* **1991**, *143* (1), 266–277.
- (46) Brenner, H. *Chem. Eng. Sci.* **1961**, *16*, 242–251.
- (47) Goren, S. I.; O'Neill, M. E. *Chem. Eng. Sci.* **1971**, *26* (3), 325–38.
- (48) Goldman, A. J.; Cox, R. G.; Brenner, H. *Chem. Eng. Sci.* **1967**, *22*, 637–651.
- (49) Goldman, A. J.; Cox, R. G.; Brenner, H. *Chem. Eng. Sci.* **1967**, *22*, 653–660.
- (50) Spielman, L. A., Particle capture from low-speed laminar flows. In *Annual review of fluid mechanics*, Vol.9, Annual Reviews: Palo Alto, CA, USA, 1977; p 297–319.
- (51) Spielman, L. A.; Cukor, P. M. *J. Colloid Interface Sci.* **1973**, *43* (1), 51–65.